

Imaging in UWB Sensor Networks

Ole Hirsch, Rudolf Zetik, and Reiner S. Thomä
*Technische Universität Ilmenau
Germany*

1. Introduction

Sensor networks consist of a number of spatially distributed nodes. These nodes perform measurements and collect information about their surrounding. They transfer data to neighboring nodes or to a data fusion center. Often measurements are performed in cooperation of several nodes.

If the network consists of Ultra-Wideband (UWB) radar sensors, the network infrastructure can be used for a rough imaging of the surrounding. In this way bigger objects (walls, pillars, machines, furniture) can be detected and their position and shape can be estimated. These are valuable information for the autonomous orientation of robots and for the inspection of buildings, especially in case of dangerous environments (fire, smoke, dust, dangerous gases). Applications of UWB sensor networks are summarized in Thomä (2007).

In this article basic aspects of imaging in UWB sensor networks are discussed. We start with a brief description of two types of UWB radar devices: impulse radar and Noise/M-sequence radar. Network imaging is based on principles of Synthetic Aperture Radar (SAR). Starting from SAR some special aspects of imaging in networks are explained in section 3. Sections 4 and 5 form the main part of the article. Here two different imaging approaches are described in more detail. The first method is multistatic imaging, i.e. the measurements are performed in cooperation of several sensor nodes at fixed places and one mobile node. The second approach is imaging by an autonomous mobile sensor, equipped with one Tx and two Rx units. This sensor uses a network of fixed nodes for its own orientation.

Part of the described methods have been practically realized in a laboratory environment. Hence, practical examples support the presentation. Conclusions and references complete the article.

2. Ultra Wideband (UWB) Radar

2.1 Main Characteristics

The main characteristic of UWB technology is the use of a very wide frequency range. A system is referred to as UWB system if it operates in a frequency band of more than 500 MHz width, or if the fractional bandwidth $bw_f = 100\% \cdot (f_H - f_L) / f_C$ is larger than 25%. Here f_H , f_L , and f_C denote the upper and lower frequency limit and the centre frequency, respectively. For imaging applications the large bandwidth is of interest because it guarantees a high resolution in range direction, as explained in the next section. UWB systems always coexist with other radio services, operating in the same frequency range. To avoid interference, a number of frequency masks and power restrictions have been agreed internationally. Current regulations are summarized in FCC (2002); Luediger & Kallenborn (2009).

A number of principles for UWB radar systems have been proposed (see Sachs et al. (2003)). In the rest of this section we briefly describe the two dominant methods 'Impulse Radar' and 'M-Sequence Radar'.

2.2 Impulse Radar

An Impulse radar measures distances by transmission of single RF pulses and subsequent reception of echo signals. The frequency spectrum of an electric pulse covers a bandwidth which is inversely proportional to its duration. To achieve ultra-wide bandwidth, the single pulses generated in an impulse radar must have a duration of $t_{\text{pulse}} \approx 1\text{ns}$ or even less. They can be generated by means of switching diodes, transistors or even laser-actuated semiconductor switches, see Hussain (1998) for an overview. Pulse shaping is required to adapt the frequency spectrum to common frequency masks. The principle of an impulse radar is shown in Fig. 1.

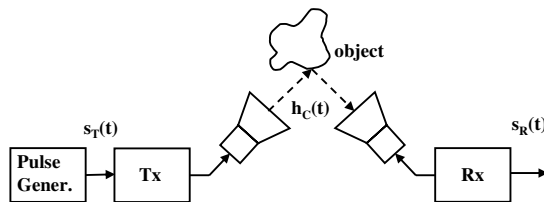


Fig. 1. Principle of an impulse radar.

The transmitter signal $s_T(t)$ is radiated by the Tx-antenna. The received signal $s_R(t)$ consists of a small fraction of the transmitted energy that was scattered at the object. $s_R(t)$ can be calculated by convolution of $s_T(t)$ with the channel impulse response $h_C(t)$:

$$s_R(t) = \int_{-\infty}^{\infty} h_C(t') \cdot s_T(t - t') dt'. \quad (1)$$

Determination of the channel impulse response is possible via de-convolution, favourably performed with the Fourier-transformed quantities $S_R(\omega), S_T(\omega)$ in the frequency domain:

$$h_C(t) = \mathcal{F}^{-1} \left\{ \frac{S_R(\omega)}{S_T(\omega)} \cdot F(\omega) \right\}. \quad (2)$$

$F(\omega)$ is a bandpass filter that suppresses high amplitudes at the edges of the frequency band, and \mathcal{F}^{-1} symbolizes the inverse Fourier transform.

The minimum delay between two subsequent pulses (repetition time t_{rep}) is given by $t_{\text{rep}} = d_{\text{max}}/c$, where d_{max} is the maximum propagation distance and c is the speed of light. For smaller pulse distances no unique identification of pulse propagation times would be possible, especially in the case of more than one object. The necessity to introduce t_{rep} limits the average signal energy since only a fraction $t_{\text{pulse}}/t_{\text{rep}}$ of the total measurement time is used for transmission and the signal peak amplitude must not exceed the allowed power restrictions. Advantageously, the temporal shift between transmission and reception of signals reduces the problem of Tx/Rx crosstalk.

2.3 Noise Radar and M-Sequence Radar

Noise signals can possess a frequency spectrum which is as wide as the spectrum of a single short pulse. Because of random phase relations between the single Fourier components the signal energy of a noise signal is distributed over the entire time axis. Signals of this kind can be used in radar systems and an example is shown in Fig. 2.

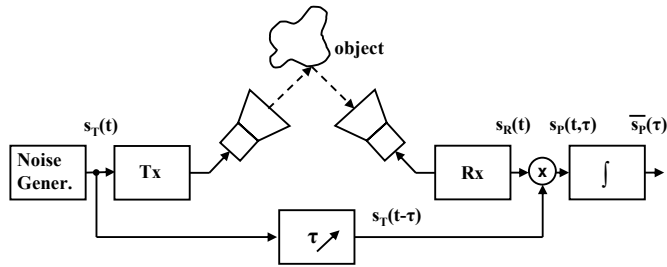


Fig. 2. Principle of a noise radar.

The relation between $s_R(t)$, $h_C(t)$, and $s_T(t)$ is of course the one already given in Equ. (1). In this kind of radar device, information about the propagation channel is extracted by correlation of the received signal with the transmitted $s_T(t)$. The correlator consists of a variable delay element introducing delay τ , a multiplier that produces the product signal $s_P(t, \tau)$:

$$s_P(t, \tau) = s_R(t) \cdot s_T(t - \tau) \tag{3}$$

and an integrator that forms the signal average for one particular τ over all t . Introduction of the convolution integral (1) into (3) and averaging over a time interval that is long in comparison to usual signal variations gives the following expression for the averaged signal $\overline{s_P}(\tau)$:

$$\overline{s_P}(\tau) = \lim_{T \rightarrow \infty} \frac{1}{2T} \int_{-T}^T s_R(t) \cdot s_T(t - \tau) dt = \lim_{T \rightarrow \infty} \frac{1}{2T} \int_{-T}^T \int_{-\infty}^{\infty} h_C(t') \cdot s_T(t - t') \cdot s_T(t - \tau) dt' dt. \tag{4}$$

In case of white noise the average value of the product $s_T(t - t') \cdot s_T(t - \tau)$ is always zero, except for $t' = \tau$. This means the autocorrelation function of white noise is a δ -function. So we can perform the following substitution:

$$\lim_{T \rightarrow \infty} \frac{1}{2T} \int_{-T}^T s_T(t - t') \cdot s_T(t - \tau) dt = \delta(t' - \tau) \cdot \lim_{T \rightarrow \infty} \frac{1}{2T} \int_{-T}^T s_T^2(t) dt = \delta(t' - \tau) \cdot \overline{s_T^2(t)}. \tag{5}$$

Applying this result we see that the correlation of noise excitation $s_T(t)$ and receiver signal $s_R(t)$ delivers the channel impulse response $h_C(t)$ multiplied by a constant factor. This factor is the square of the effective value of $s_T(t)$:

$$\overline{s_P}(\tau) = \overline{s_T^2(t)} \int_{-\infty}^{\infty} h_C(t') \cdot \delta(t' - \tau) dt' = \overline{s_T^2(t)} \cdot h_C(\tau). \tag{6}$$

An M-sequence radar is a special form of a noise radar, where $s_T(t)$ consists of a maximum length binary sequence, see Sachs (2004) for details. This pseudo-stochastic signal is generated in a shift register with feedback. Both noise radar and M-sequence radar use the full measurement duration for transmission and reception of signals, maximizing the UWB signal energy in this way. Decoupling between transmitter and receiver becomes more important since Tx and Rx operate at the same time.

3. Specifics of Imaging in Sensor Networks

3.1 Synthetic Aperture Radar (SAR)

Imaging in sensor networks is based on results of conventional microwave imaging, i.e. imaging with only one single Tx/Rx antenna pair. Especially the principles of "Synthetic Aperture Radar" (SAR) can be adapted to the special needs of sensor network imaging. Instead of using an antenna with a large aperture, here the aperture is synthesized by movement of antennas and sequential data acquisition from different positions. For an overview of SAR imaging see Oliver (1989), and for a typical UWB-SAR application see Gu et al. (2004). In 3.3 relations between the length of the scan path (aperture) and image resolution are explained. To achieve reasonable resolution, the antenna aperture of a radar imaging system must be significantly bigger than the wavelength λ . Processing of SAR data is explained in connection with general processing in 4.1 .

3.2 Arrangement of Network Nodes and Scan Path

The network consists of a number of nodes. These are individual sensors with Rx and/or Tx capabilities. Specialized nodes can collect data from several other nodes, and typically one node forms the fusion center, where the image is computed from the totality of the acquired data.

The network can be completed by so called 'anchor nodes'. These are nodes at known, fixed positions. Primarily they support position estimation of the mobile nodes, but additionally they can be employed in the imaging process.

The spatial arrangement of network nodes (network topology) strongly influences the performance of an imaging network. Together topology and scan path must guarantee that all objects are illuminated by the Tx antennas and that a significant part of the scattered radiation can be collected by the Rx antennas.

A number of frequently chosen scan geometries (node positions and scan paths) are shown in Fig. 3. At least one antenna must move during the measurement; or an array of antennas has to be used, as in Fig. 3(b). Two main cases can be distinguished with respect to the scan path selection:

1. The object positions are already known. In this case imaging shall give information on the shape of objects and small modifications of their position.
2. The object positions are entirely unknown. In this case a rough image of the entire surrounding has to be created.

The optimum scan geometry is concave shaped in case 1, e.g. Fig. 3(b) and (c). This shape guarantees that the antennas are always directed towards the objects, so that a significant part of the scattered radiation is received. If the region of interest is accessible from one side only, then semi circle or linear scan geometries are appropriate choices.

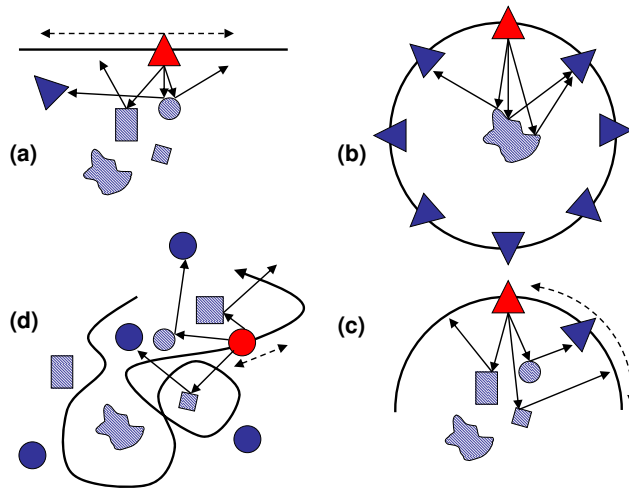


Fig. 3. Typical scan geometries in imaging sensor networks: (a) linear scan, (b) full circle, (c) semi circle, (d) arbitrary scan path. Filled triangles and circles: antennas, hatched figures: objects.

In entirely unknown environment a previous optimization of node positions is not possible. In this case the nodes are placed at random positions. They should have similar mutual distances. Node positioning can be improved after initial measurements, if some nodes don't receive sufficient signals. A network of randomly placed nodes requires the use of omnidirectional antennas, which can cause a reduction of the signal to clutter ration in comparison to directional antennas.

3.3 Resolution

Resolution is a measure of up to which distance two closely spaced objects are still imaged separately. In radar technique we must distinguish between 'range resolution' ρ_z (along the direction of wave propagation) and 'cross range resolution' ρ_x (perpendicular to the direction of propagation). An approximation for the former is:

$$\rho_z \approx \frac{c}{2bw}. \quad (7)$$

It is immediately understandable that ρ_z improves with the bandwidth bw because the speed of light c divided by bw is a measure for the width of the propagating wave packet in the spatial domain. The '2' results from two times passage of the geometrical distance in radar measurements.

A rough estimation of cross range resolution ρ_x can be derived by means of Fig. 4. d and d_1 are the path lengths to the end points of ρ_x when the antenna is at one end position of the aperture A . We assume the criterion that two neighbouring points can be resolved if a path difference $\Delta d = d - d_1$ of the order of half the wavelength λ appears during movement of the antenna along the aperture A , resulting in a signal phase difference of $\approx 2\pi$ (two way propagation). Typically the distances are related to each other as follows: $A \gg \rho_x$, $R \gg \rho_x$, $R > A$. Under

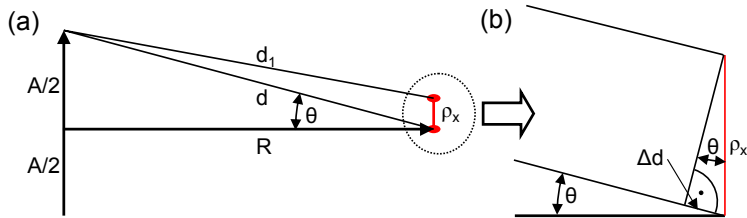


Fig. 4. Approximation of cross range resolution ρ_x . (b) is a zoomed version of the encircled section in (a).

these circumstances d and d_1 can be assumed as being parallel on short lengthscales. The angle θ appears both in the small triangle with sides ρ_x and Δd , and in the big triangle with half aperture $A/2$ and range R :

$$\sin \theta = \frac{\Delta d}{\rho_x}, \quad \tan \theta = \frac{A/2}{R} \quad . \quad (8)$$

After rearranging of both equations, insertion into each other, and application of the relation $\sin(\arctan(x)) = x/\sqrt{1+x^2}$ we get an expression for ρ_x :

$$\rho_x = \frac{\Delta d \cdot 2R \cdot \sqrt{1 + (A/(2R))^2}}{2A} \approx \frac{\lambda R}{2A} \quad . \quad (9)$$

Here Δd was replaced by $\lambda/2$. The extra '2' in the denominator results from the fact that the calculation was performed with only half the actual aperture length. With the assumed relation between A and R the square root expression can be set to 1 in this approximation. While range resolution depends on the bandwidth, cross range resolution is mainly dependent on the ratio between aperture and wavelength. In UWB systems resolution is estimated with an average wavelength. In imaging networks the two cases 'range' and 'cross range' are always mixed. For a proper resolution approximation the node arrangement and the signal pulse shape must be taken into account.

3.4 Localization of Nodes and Temporal Synchronization

Imaging-algorithms need the distance Tx \rightarrow object \rightarrow Rx at each position of the mobile nodes. This requires knowledge of all anchor node positions and continuous tracking of the mobile nodes. Time-based node localization is possible only with exact temporal synchronization of the single nodes.

3.4.1 Localization of Nodes

Before we list the different localization tasks, we introduce abbreviations for the localization methods:

- TOA: Time of arrival ranging/localization
- TDOA: Time difference of arrival localization
- AOA: Angle of arrival localization
- ADOA: Angle difference of arrival localization

- RTT: Round trip time ranging
- RSS: Received signal strength ranging

It is not necessary to explain these methods here, because this subject is covered in the literature extensively. Summaries can be found in Patwari et al. (2005) and in Sayed et al. (2005). AOA and ADOA methods are explained in Rong & Sichertiu (2006), and TDOA methods are discussed in Stoica & Li (2006).

The single tasks are:

1. The positions of the static nodes (anchor nodes) must be estimated. If the network is a fixed installation, then this task is already fulfilled. Otherwise anchor node positions can be found by means of TOA localization (if synchronization is available) or by means of RTT estimations (synchronization not required).
2. The positions of mobile nodes must be tracked continuously. If the sensors move along predefined paths, then their positions are known in advance. In case of synchronization between mobile nodes and anchors, position estimation is possible with TOA methods. Without synchronization node positions may be found by TDOA, AOA, or ADOA methods. RSS is not very precise; RTT could be used in principle but requires much effort.

Methods that involve angle measurements (AOA and ADOA) can only be performed if the sensor is equipped with directional antennas or with an antenna array. Time-based methods require exact synchronization; in case of TDOA only on the individual sensor platform, for TOA and RTT within the network. The large bandwidth and good temporal resolution of UWB systems are huge advantages for time-based position measurements.

3.4.2 Temporal Synchronization of Network Nodes

Two main reasons exist for temporal synchronization of network nodes:

1. Application of time-based localization methods.
2. Use of correlation receivers in M-sequence systems.

Point 1 was already discussed. The necessity of synchronization in networks with correlation receivers can be seen from Fig. 5.

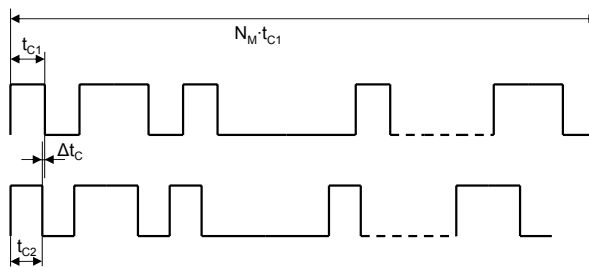


Fig. 5. Mismatch between a received M-sequence signal and the reference signal because of differing clock frequencies $1/t_{c1}$ and $1/t_{c2}$ of Tx and Rx. The total time shift is $N_M \cdot \Delta t_C$ (N_M : Number of chips; Δt_C : time difference per cycle).

Over the sequence duration of $N_M \cdot t_{C1}$ a maximum shift of $\approx \frac{1}{2}t_{C1}$ is tolerable. This corresponds to a maximum clock frequency difference of

$$\Delta f_C < \frac{1}{2N_M} f_{C1} \quad . \quad (10)$$

A comprehensive introduction into synchronization methods and protocols is given in Serpedin & Chaudhari (2009). Originally, many of these methods were developed for communications networks. The good time resolution of UWB signals makes them a candidate for synchronization tasks. An example is given in Yang & Yang (2006).

3.5 Data Fusion

Processing of data in an imaging sensor network is distributed across the nodes. Part of the processing steps are performed at the individual sensors while, after a data transfer, final processing is done at the fusion center. An example flow chart is shown in Fig. 6.

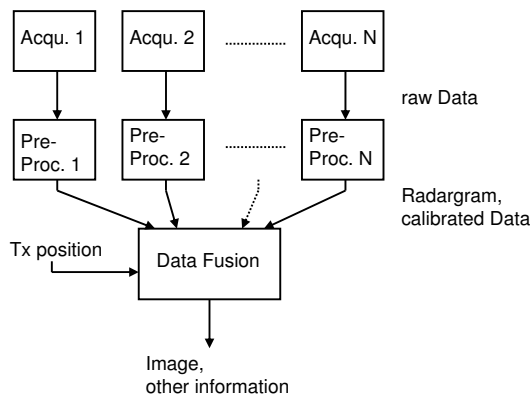


Fig. 6. Data processing in a network with one Tx and N Rx. The single steps are Data acquisition (Acqu.), Pre-processing (Pre-Proc.), and Data Fusion.

After transmitting a pulse or an M-sequence by the Tx, data are acquired by the Rx hardware. Typically the sensor hardware performs some additional tasks: analog to digital conversion, correlation with a known signal pattern (in case of M-sequence systems), and accumulation of measurements to improve the signal to noise ratio.

The next step is pre-processing of the raw data, usually performed in a signal processor at the sensor node. De-convolution of raw data with a measured calibration function can increase the usable bandwidth and in this way it can increase range resolution. In M-sequence systems data must be shifted to achieve coincidence between the moment of signal transmission and receiver time zero (Sachs (2004)). The result of pre-processing can be visualized in a radargram (Fig. 15). It displays the processed signals in form of vertical traces against the 'slow' time dimension of sensor movement. For some analyses only the TOA of the first echo is of importance. Then pre-processing includes a discrimination step, which reduces the information to a single TOA value.

Data fusion is a generic term for methods that combine information from the single sensor nodes and produce the image. While acquisition and pre-processing don't vary a lot between

the different imaging methods, data fusion is strongly dependent on network topology, sensor pathways, and imaging method. Examples are described in section 4.

Additional information, required for imaging, are the positions of mobile nodes. As long as the sensors follow predetermined pathways, this information is always available. In other cases the mobile node positions must be estimated by means of mechanical sensors or the position is extracted from radar signals.

Fusion is not always the last processing step. By application of image processing methods supplementary information can be extracted from the radar image.

4. Imaging in Distributed Multistatic Networks

4.1 Multistatic SAR Imaging

The multitude of different propagation pathways in a distributed sensor network can be used for rough imaging of the environment. A signal, transmitted by a Tx, is reflected or scattered at walls, furniture, and other objects. The individual Rx receive these scattered signals from different perspectives. The information about the object position is contained in the signal propagation times. The principle of this method is shown in Fig. 7. The propagation paths are sketched for a signal scattered at an objects corner. In principle, the positions of Tx and Rx could be swapped, but an arrangement with only one Tx and several Rx has the advantage of simultaneous operation of all Rx.

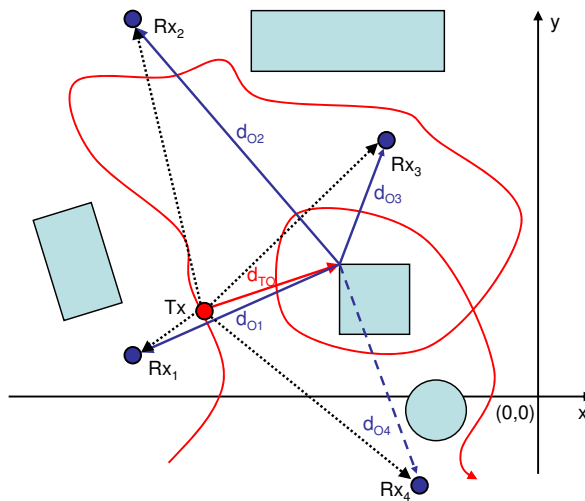


Fig. 7. Principle of imaging in a multistatic network. The four receivers (Rx_i) are placed at fixed positions. The Transmitter (Tx) moves along the curved pathway.

Prerequisites for application of this method are knowledge of the Rx positions, temporal synchronization of all nodes, and application of omnidirectional antennas. The synthetic aperture has the shape of an arbitrary path through the environment. Data acquisition is carried out as follows:

- The Tx moves through the region. It transmits signals every few centimeters.

- All Rx receive the scattered signals. From the totality of received signals a radargram can be drawn for each Rx.

The recorded data are processed in two ways:

- The Tx position at the individual measurement points are reconstructed from the LOS signals between Tx and Rx (dotted lines in Fig. 7).
- The image is computed by means of a simple migration algorithm.

Separately for each receiver Rx_i an image is computed. The brightness in one point $B_i(x, y)$ is the coherent sum of all signals s_r , originating from the scatterer at position (x, y) , summarized along the aperture (n is the number of the measurement along the Tx path).

$$B_i(x, y) = \sum_{n=1}^N s_r(\tau_{in}, n). \quad (11)$$

The delay τ_{in} is the time required for wave propagation along the way $Tx \rightarrow$ object point $(x, y) \rightarrow Rx_i$ with speed c :

$$\tau_{in} = \frac{1}{c}(d_{TO}(n) + d_{Oi}) = \frac{1}{c} \left(\sqrt{(x - x_{Tx}(n))^2 + (y - y_{Tx}(n))^2} + \sqrt{(x_{Rx_i} - x)^2 + (y_{Rx_i} - y)^2} \right). \quad (12)$$

The meaning of the used symbols can be seen from Fig. 7. This migration algorithm summarizes signals along ellipses, which have their foci at the respective Tx and Rx position. The ellipses for all possible Tx-Rx constellations have in common that they touch the considered object point.

For improved performance, migration algorithms, based on wave equations must be applied, see Margrave (2001). Stolt Migration, computed in the wavenumber-domain, is a fast migration method (Stolt (1978)). However, it requires an equally spaced net of sampling points. Therefore it cannot be applied in case of an arbitrary-shaped scan path.

4.2 Cross-Correlated Imaging

The summation, mentioned in the previous section, cumulates intensity of the image at positions, where objects, which evoked echoes in measured impulse responses, are present. However, this simple addition of multiple snapshots also creates disturbing artefacts in the focused image (see Fig. 9(a)). The elliptical traces do not only intersect at object's positions. They intersect also at other positions and even the ellipsis themselves make the image interpretation difficult or impossible.

In order to reduce these artefacts, a method based on cross-correlated back projection was proposed in Foo & Kashyap (2004). This method suggests a modification of the snapshot's computation. Instead of a simple remapping of an impulse response signal the modified snapshot is created by a cross-correlation of two impulse responses:

$$B(x, y) = \frac{1}{N} \sum_{n=1}^N \int_{-T/2}^{T/2} s_r \left(\frac{d_{TO}(n) + d_{Oi}}{c} + \xi \right) s_{ref} \left(\frac{d_{TO}(n) + d_{Oiref}}{c} + \xi \right) d\xi, \quad (13)$$

where s_{ref} is an impulse response measured by an auxiliary reference receiver at a suitable measurement position. Since two different delay terms $(d_{TO}(n) + d_{Oi})/c$ and $(d_{TO}(n) + d_{Oiref})/c$ have to match the actual scattering scenario in conjunction, the probability to add

"wrong" energy to an image pixel (x,y) , which does not coincide with an object, will be reduced. The integration interval T is chosen to match the duration of the stimulation impulse. Further improvement of this method was proposed in Zetik et al. (2005a); Zetik et al. (2005b); and Zetik et al. (2008). The first two references introduce modifications that improve the performance of the cross-correlated back projection from Foo & Kashyap (2004) by additional reference nodes. This drastically reduces artefacts in the focused image. In Zetik et al. (2008), a generalised form of the imaging algorithm, which is suitable for application in distributed sensor networks, is proposed:

$$B(x,y) = \frac{1}{N} \sum_{n=1}^N W_n(x,y) A[s_{rn}(x,y), s_{ref1n}(x,y), \dots, s_{refMn}(x,y)] \quad , \quad (14)$$

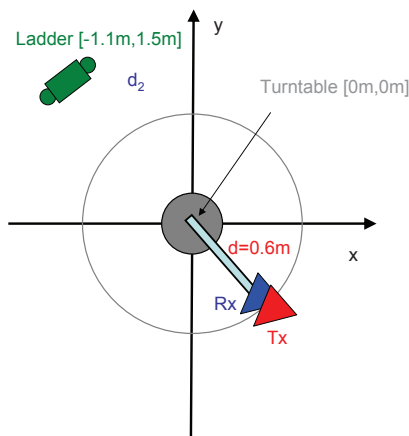


Fig. 8. Cross-correlated imaging with a circular aperture. The data measured at a certain position are multiplied with reference data, acquired at a position with 120° offset.

where $A[\cdot]$ is an operator, which averages N spatially distributed observations and $W_n(x,y)$ are weighing coefficients. It is assumed that all N averaged nodes can "see" an object at the position (x,y) . In case of point-like objects, the incident EM waves are scattered in all directions. Hence, sensor nodes can be arbitrarily situated around the position (x,y) and they will still "see" an object (if there is one). However, extended objects, such as walls, reflect EM waves like a mirror. A sensor node can "see" only a small part of this object, which is observed under the perpendicular viewing angle. Therefore, the selection of the additional reference nodes must be done very carefully. A proper selection of sensor nodes for point like and also distributed objects is discussed in detail in Zetik et al. (2008). The weighting coefficients $W_n(x,y)$ are inversely related to the number of nodes (measurement positions) that observe a specific part in the focused image. This reduces over and under illumination of the focused image by taking into account the topology of the network.

The following measured example demonstrates differences between images obtained by the conventional SAR algorithm (11) and the cross-correlated algorithm (14). The measurement constellation is shown in Fig. 8. The target - a metallic ladder - was observed by a sensor, which was moving along a circular track in its vicinity. The sensor comprised two closely

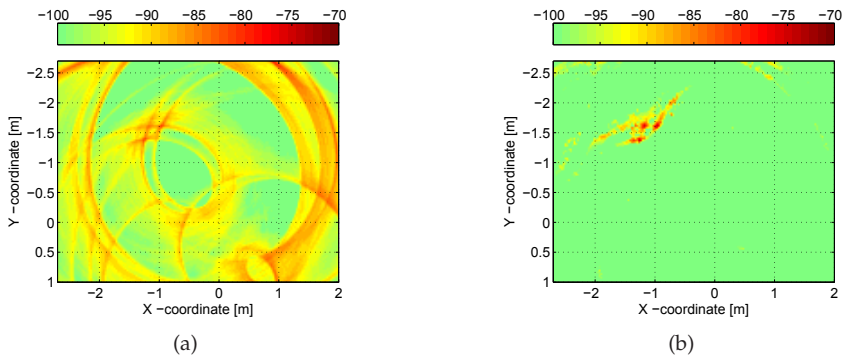


Fig. 9. (a) Image taken with the arrangement shown in Fig. 8 and processed with conventional migration algorithm. (b) Image processed with cross-correlated migration algorithm.

spaced antennas. One antenna was transmitting an UWB signal covering a bandwidth from 3.5 to 10.5 GHz. The second antenna was receiving signals reflected from the surroundings. Both antennas were mounted on the arm attached to the turntable. About 800 impulse responses were recorded. The origin of the local coordinate system was selected to be the middle of the turntable.

Firstly, the measured impulse responses were fused by the conventional SAR algorithm (11). The result of this imaging on a logarithmical scale is depicted in Fig. 9(a). The whole image is distorted by data fusion artefacts and is hard to interpret. The result can be improved by the generalised imaging algorithm (14). Here, the operator $A[.]$ was replaced by the minimum value operator. It took the minimum magnitude from 3 observations s_{rn} , s_{ref1n} and s_{ref2n} . The position of two additional reference nodes Rref1n and Rref2n was computed adaptively for each pixel (x,y) of the focused image and to each measured impulse response R_n . The adaptation criterion was the 120° difference in the viewing angles of all 3 nodes. The reduction of disturbing artefacts is evident in Fig. 9(b).

4.3 Indirect Imaging of Objects

The procedure explained in 4.1 can be 'reversed'. Instead of measuring the signals reflected at objects, indirect imaging detects free LOS paths between objects within the area of interest. An example is shown in Fig. 10. Generally a network of anchor nodes is required. First these anchors estimate their respective positions and, later on, they operate as Rx nodes at fixed positions. A mobile Tx moves around the area of objects and anchor nodes. The Tx emits UWB signals which are received at all Rx nodes. From the received signals two kinds of information are extracted: the propagation time, which is a measure for the current Tx-Rx distance, and the information about LOS or NLOS between Tx and Rx. The path of the Tx can be reconstructed from the totality of distance estimates. The second information allows creation of a map of LOS paths between the Tx path and the respective Rx position. An overlay of all individual LOS path maps reveals positions and approximate contours of the objects. Diffraction at the edges of objects limits the performance of the described procedure and causes a underestimation of object dimensions. The method is explained in more detail in Hirsch et al. (2010).

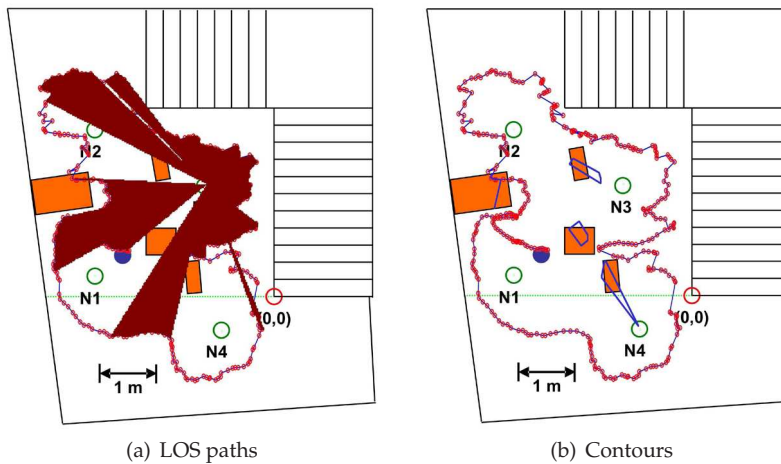


Fig. 10. Indirect Imaging of objects. (a) LOS paths (dark regions) between the Tx pathway (small circles) and Rx node 3. (b) Position of objects (filled boxes) and estimated object contours (open boxes).

5. Imaging by Autonomous Rotating Sensors within a Network

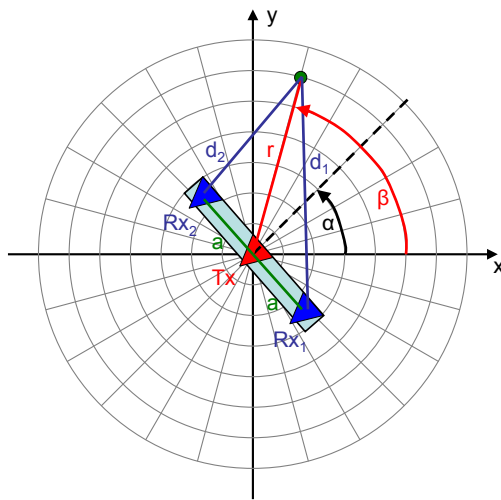
5.1 Design

The networks presented in the previous sections consist of a number of nodes at fixed positions and one mobile node that moves along the imaging aperture. The imaging process requires cooperation of all nodes. Now we introduce a sensor that autonomously operates within a network of anchor nodes. It consists of a mobile platform equipped with one Tx and two Rx units and with the corresponding antennas. The sensor can move within the area of the network, varying its perspective in this way; and it can rotate to acquire 360° panoramic views. Because of the similarity to the ultrasound locating system of a bat we call it a bat-type sensor. By means of the anchor nodes the bat sensor can estimate its own position and its present orientation. Fig. 11 shows the geometry and a laboratory prototype. In principle the anchor nodes could be used as additional 'illuminators' or as additional receivers. These aspects were not investigated in the frame of this work.

5.2 Orientation within the Network

An image of the environment is typically assembled from several individual measurements performed with the bat-type sensor at different locations. For the correct assignment of these images the position and orientation of the sensor within the room must be estimated. As long as temporal synchronization exists between the network of anchor nodes and the bat-type sensor, a variety of time of arrival (TOA) localization methods can be applied for this purpose.

Here we present a method that neither requires temporal synchronization between mobile sensor and anchor nodes nor synchronization within the network of anchor nodes. It is based on angle measurements and can be classified as 'angle difference of arrival' (ADOA) localization. Line of sight from the mobile sensor to at least three anchor nodes is required. The basic idea consists in establishment of a system of two equations, where the input parameters



(a) Geometry



(b) Prototype

Fig. 11. Geometry and laboratory prototype of a bat-type sensor. The point, where r , d_1 , and d_2 come together, is an object point.

are the known positions of the anchor nodes and the difference angles between three anchor node directions, measured by the bat-type sensor. The solutions are the x - and y -position of the mobile sensor. Afterwards the sensor orientation can be estimated.

The situation is sketched in Fig. 12. We distinguish between the global coordinate system (x_g, y_g) , defined by anchor nodes A_1, A_2, A_3 , and the coordinate system of the bat-type sensor, which has its origin at coordinates (x_b, y_b) within the global system and which is rotated against that system by α_b . The mathematical effort is reduced if the global system is arranged in such a way that one node forms the origin and another node is placed directly on one coordinate axis. This choice does not reduce the generality of the method.

All anchor nodes operate in Tx mode. Then the bat sensor can easily estimate the direction angles to this nodes $\alpha_1, \alpha_2, \alpha_3$ within its own coordinate system. During a sensor rotation the signal strength reaches a maximum at rotation angles where the sensor antennas are directed towards an anchor node. These angles can be extracted from the radargram with good accuracy because the TOA traces of left and right Rx antenna intersect at the transmitter positions, see Fig. 15. Because of the unknown α_b this information is not directly usable for position estimation but the angle differences $\alpha_{12} = \alpha_2 - \alpha_1$ and $\alpha_{31} = \alpha_1 - \alpha_3$ can be used, since they remain the same in both coordinate systems.

a_1, a_2, a_3 form the connection lines between sensor position (x_b, y_b) and the anchor nodes; and α_{12}, α_{31} represent the cutting angles between these lines. Now we establish the system of equations, which connects the cutting angles with the slopes m_i of the connection lines:

$$\tan \alpha_{12} = \frac{m_2 - m_1}{1 + m_2 m_1}, \quad \tan \alpha_{31} = \frac{m_1 - m_3}{1 + m_1 m_3} \quad (15)$$

The slopes follow from the anchor node coordinates and from the bat-type sensor position:

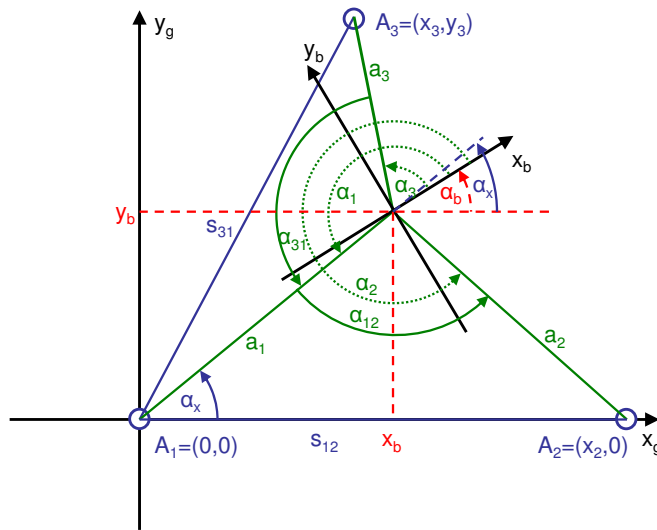


Fig. 12. Estimation of position (x_b, y_b) and orientation (α_b) of a bat-type sensor within the global coordinate system (x_g, y_g) . See text for details.

$$m_1 = \frac{y_b}{x_b}, \quad m_2 = \frac{-y_b}{x_2 - x_b}, \quad m_3 = \frac{y_3 - y_b}{x_3 - x_b} \quad (16)$$

Insertion of (16) in (15), expansion of the resulting expressions, and summary of the coefficients of x_b and y_b , respectively, delivers the following system of equations:

$$x_b^2 + y_b^2 = x_2 x_b + \frac{x_2}{\tan \alpha_{12}} y_b, \quad x_b^2 + y_b^2 = \left(x_3 + \frac{y_3}{\tan \alpha_{31}} \right) x_b + \left(y_3 - \frac{x_3}{\tan \alpha_{31}} \right) y_b \quad (17)$$

Equalization of the two equations (17) gives the following expression, where we introduce the abbreviations S and T:

$$0 = \left(-x_2 + x_3 + \frac{y_3}{\tan \alpha_{31}} \right) x_b + \left(y_3 - \frac{x_3}{\tan \alpha_{31}} - \frac{x_2}{\tan \alpha_{12}} \right) y_b = Sx_b + Ty_b \quad (18)$$

In this way we have found expressions for y_b and y_b^2 :

$$y_b = -\frac{S}{T} x_b, \quad y_b^2 = \left(\frac{S}{T} \right)^2 x_b^2 \quad (19)$$

Introduction of (19) in the first equation (17) gives a formula for x_b :

$$x_b = x_2 \left(1 - \frac{S}{\tan \alpha_{12} T} \right) / \left(1 + \left(\frac{S}{T} \right)^2 \right) \quad (20)$$

Finally the orientation of the bat-type sensor is calculated. The angle between a_1 and the x-axis is $\alpha_x = \arctan(y_b/x_b)$. From Fig. 12 one can see that the orientation angle α_b must be:

$$\alpha_b = \alpha_x - \alpha_1 + \pi \quad (21)$$

An alternative angle of arrival (AOA) localization method, employing pairs of angle measurements between neighbor nodes, is described in Rong & Sichertiu (2006).

5.3 Calculation of Echo Profiles

In this section we calculate the signal propagation time for the paths from the Tx via the object to the Rx. The sensor acquires data during a full rotation. That's why the radar propagation time follows a systematic dependency. Knowledge of this dependency is required for the design of signal processing and focus algorithms. Additionally, the calculation delivers the angles of incidence both for the Tx and for the Rx antenna for each azimuth angle of the bat sensor. This allows inclusion of the antenna characteristics in the calculation of profiles of signal intensity vs. azimuth angle. Such profiles are valuable for classification of reflecting objects, for calculation of the field of view, and for the estimation of cross-range resolution.

The use of polar coordinates is convenient because of the rotational symmetry of the arrangement. The object coordinates are azimuth β and radius r . The bat sensor azimuth angle is α . In the initial sensor position the bar with the 3 antennas is aligned along the y-axis. In this position α is 0 and the sensor is looking towards the positive x-axis. The sensor rotates counter-clockwise (positive sense of rotation).

First we consider the simpler case of signal reflection at a point-like object, shown in Fig. 11(a). Because the Tx antenna is placed in the origin of the local bat coordinate system, r (the distance Tx-object) does not depend on α . The length of d_1 and d_2 (distances object-Rx₁, Rx₂) are determined by the oblique-angled triangles consisting of radius r , the arm of length a , and d_1 or d_2 . The law of cosines is applied to find d_1 and d_2 in these triangles (in '±' or '∓' the upper sign is always valid for index 1 while the lower sign is valid for index 2):

$$d_{1/2} = \sqrt{a^2 + r^2 - 2 a r \cos(\pi/2 \pm (\beta - \alpha))} \quad (22)$$

Then the total propagation times are:

$$\tau_{1/2}(\alpha) = (1/c) \cdot (r + d_{1/2}(\alpha)) \quad (23)$$

In radar imaging objects are often treated as if they were composed of single point scatterers. This is a simplification and fails in the case of bigger objects. In case of objects that are significantly bigger than the wavelength specular reflection dominates. From this reason we now consider the case of a reflection at a wall, which represents the extreme case of a spacious object and is more realistic than the point scatterer model in indoor imaging applications. A sketch of a bat sensor in front of a wall is shown in Fig. 13.

For convenience we use an azimuth angle δ that is $\pi/2 - \alpha$. In this way the sensor orientation is parallel to the wall at $\delta = 0$. In case of the wall reflection the point where the reflection occurs is not further fixed. Instead it moves during the rotation of the sensor. By means of the geometric construction in Fig. 13 those paths are to be found, which connect Tx and Rx_{1/2} after a reflection at the wall and which fulfill the law of reflection at the same time. This law states that the angle of incidence is equal to the reflection angle. Then in our construction the perpendicular from the reflection point separates the x-axis in two regions of equal lengths s_{x1} and s_{x2} , respectively.

To determine the propagation path lengths $s_{T1/T2}(\delta)$ and $s_{R1/R2}(\delta)$ we first need to find the dependency of s_{x1} and s_{x2} on δ . We establish a linear equation of the general form $y = mx + n$ for the lines that contain $s_{R1/R2}$:

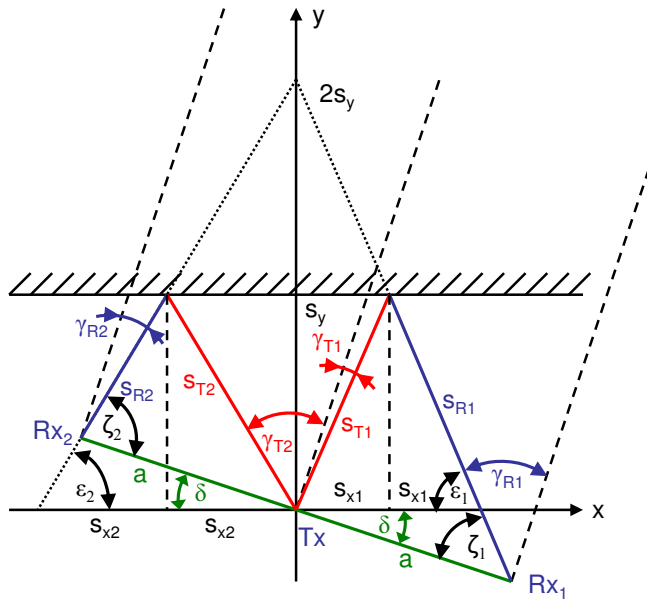


Fig. 13. Propagation paths in case of a bat sensor that rotates in front of a wall. The sensor is symbolized by the bar $Rx_1-Tx-Rx_2$. The wall goes parallel to the x -axis at a distance s_y . The antenna main lobe directions are given by the dashed lines. See text for details.

$$y = \frac{-a \sin \delta \mp 2 s_y}{a \cos \delta} x + 2 s_y \quad (24)$$

$a \cos \delta$ and $a \sin \delta$ are the projections of the bar a onto x - and y -axis. Setting $y = 0$ and rearranging Equ. (24) the intersection with the x -axis is found and in this way the length of $s_{x1/x2}$:

$$s_{x1/x2}(\delta) = \frac{s_y a \cos \delta}{a \sin \delta \pm 2 s_y} \quad (25)$$

Using this result explicit expressions for the path lengths can now be given:

$$s_{T1/T2}(\delta) = \sqrt{s_{x1/x2}^2(\delta) + s_y^2} \quad (26)$$

$$s_{R1/R2}(\delta) = \sqrt{(a \cos \delta \mp s_{x1/x2}(\delta))^2 + (s_y \pm a \sin \delta)^2} \quad (27)$$

The total propagation times $\tau_{1/2}(\delta)$ are the quotients of the total propagation distances and the speed of light:

$$\tau_{1/2}(\delta) = \frac{s_{T1/T2}(\delta) + s_{R1/R2}(\delta)}{c} \quad (28)$$

Fig. 15 illustrates this dependency on a practical example. The result of Equ. (28) is shown for azimuth angles α from 0° to 359° (remember: $\delta = \pi/2 - \alpha$). When the bat sensor is facing the

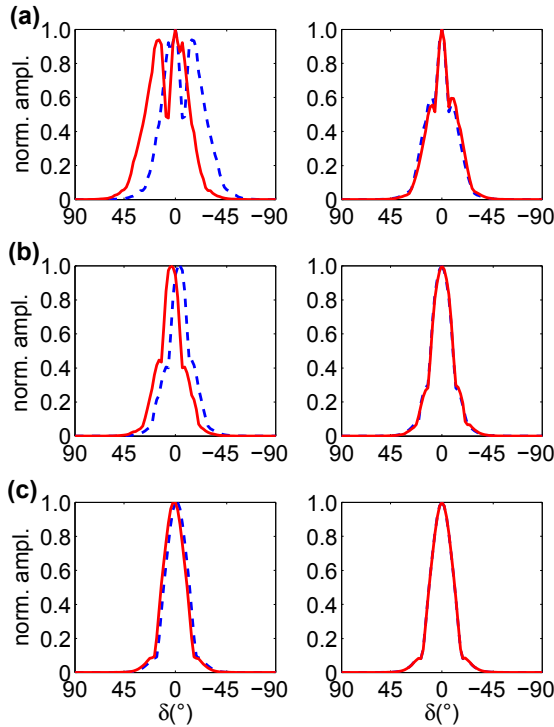


Fig. 14. Simulated amplitude vs. bat sensor rotation δ for point scatterer (left) and wall reflection (right). The length of the bat arm (variable a in Fig. 13) was 0.25 m. The distances between the center of rotation of the bat and the reflector were (a) 0.5 m, (b) 1.0 m, and (c) 5.0 m. Hatched line: signal at R_{x_1} , solid line: signal at R_{x_2} . The radiation pattern used in this simulation is the measured pattern of a double-ridge horn antenna described in Schwarz et al. (2010).

object both propagation times are equally long and the curves $\tau_{1/2}(\delta)$ intersect. The objects are visible only within a fraction of the rotation angle due to the antenna directivity. For the calculation of the angles of incidence γ we first need to determine the auxiliary angle $\varepsilon_{1/2}$, which is part of the right-angled triangle with sides s_{x_1/x_2} , s_{R_1/R_2} , and s_y . It is

$$\sin \varepsilon_{1/2}(\delta) = \frac{s_y}{s_{T_1/T_2}(\delta)} \quad (29)$$

With this result we can give expressions for the angles of emergence γ_{T_1/T_2} at the Tx antenna:

$$\gamma_{T_1/T_2}(\delta) = \frac{\pi}{2} \mp \delta - \arcsin \frac{s_y}{s_{T_1/T_2}(\delta)} \quad (30)$$

In a similar way we determine the angles of incidence γ_{R_1/R_2} at the receiver antennas. Here we have to use the auxiliary angle $\zeta_{1/2}$ that can be found from the sum of the internal angles of

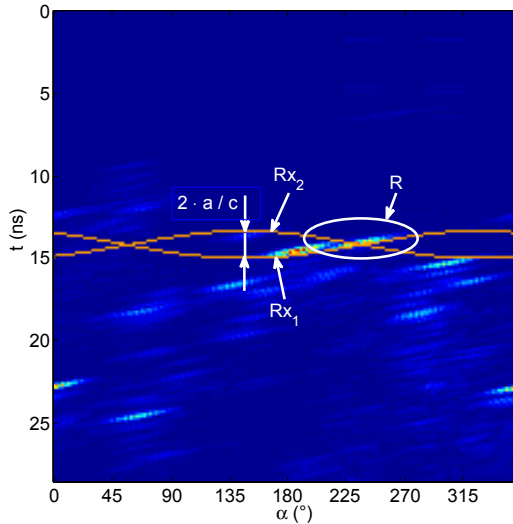


Fig. 15. Radargram of receiver Rx_1 with the curves of time of arrival (TOA) vs. bat azimuth angle α for Rx_1 and Rx_2 . The Ellipse R marks the radar reflex for which the TOA curves have been calculated.

the triangles with corner points Tx , $Rx_{1/2}$, and the intersection point of $s_{R1/R2}$ with the x-axis. For Rx_1 and Rx_2 these sums are:

$$\pi = (\pi - \varepsilon_1) + \zeta_1 + \delta \quad \pi = (\pi - \zeta_2) + \varepsilon_2 + \delta \quad . \quad (31)$$

By using these relations and Equ. (29) an expression for the angles of incidence can be given:

$$\gamma_{R1/R2}(\delta) = \frac{\pi}{2} - \zeta_{1/2}(\delta) = \frac{\pi}{2} \pm \delta - \arcsin \frac{s_y}{s_{T1/T2}(\delta)} \quad . \quad (32)$$

Now the amplitude $A_{1/2}$ of the received signal vs. the rotation angle δ can be computed. Given an antenna radiation patter $p(\gamma)$ the amplitude can be computed by a multiplication of weighting factors for the incidence at the Rx and Tx antennas and for the total propagation pathlength:

$$A_{1/2}(\delta) = p(\gamma_{R1/R2}(\delta)) \cdot p(\gamma_{T1/T2}(\delta)) \cdot \frac{s_{ref}}{s_{T1/T2}(\delta) + s_{R1/R2}(\delta)} \quad . \quad (33)$$

The reference distance s_{ref} is the total propagation distance at $\delta = 0$. In Fig. 14 results are plotted for the antenna DRH-90 (Schwarz et al. (2010)). At short distances (curves (a) and (b)) the successive appearance of the object first in the visibility range of Rx_2 and then of Rx_1 can clearly be seen. This effect is reduced in case of the wall reflection. The pattern at the largest distance (5 m) are practically identical with the square of the measured antenna radiation pattern. In this simulation the antennas are treated as point objects. This is still a simplification.

5.4 Detection of Individual Reflectors

Typically, a radar image is created from the acquired data by application of a migration algorithm. This procedure can as well be applied to the rotating bat-type sensor. In this case delays have to be calculated (similar to Equ. (12)) for both Rx separately. An example is shown in Fig. 17(b).

A disadvantage of this procedure is the appearance of parts of ellipses or circles in the final image, as they can be seen in the example. These are remains from the summation along curves. Furthermore, almost all migration algorithms were derived for point-like scatterers, but in indoor imaging most objects cause specular reflections.

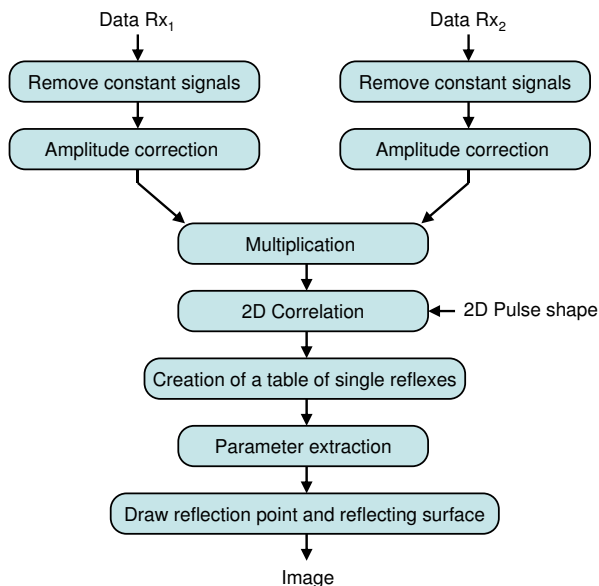
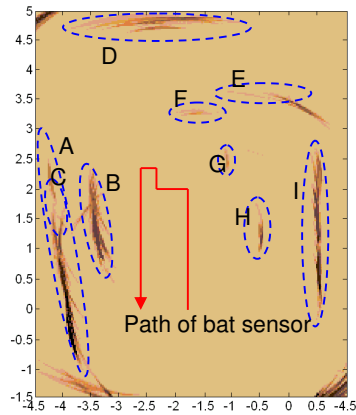


Fig. 16. Creation of an image from individual reflections at flat surfaces.

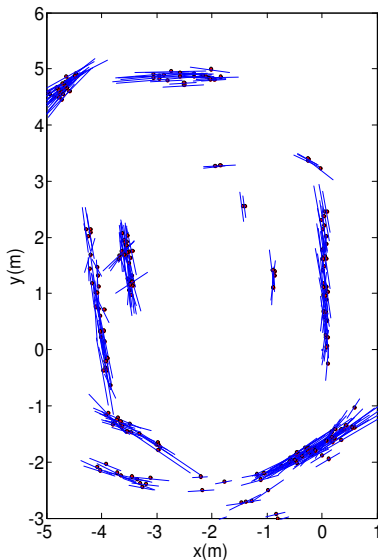
An attempt to create a more realistic final image is detection of individual flat reflectors from the radar returns. This is based on the following consideration: The reflection from a flat surface reaches a maximum when the irradiation occurs along the direction of the surface normal; from this it follows that during sensor rotation, signal maxima will occur when the sensor looks towards the surface normal of objects. Signal components that are reflected into directions far away from the surface normal cannot be detected from the bat-type sensor, because of the sensors small dimensions.



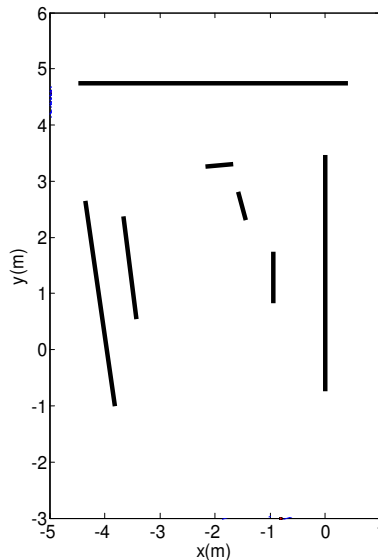
(a) Photograph



(b) Conventional processing



(c) Detection of single scatterers.



(d) Schematic representation of reflecting surfaces.

Fig. 17. Imaging with bat-type sensor in a stairwell. The images show an overlay of 15 measurement results, performed along the marked sensor path.

Now each reflex in the radargram can be interpreted as a flat surface fragment. The center of gravity of the reflex delivers the coordinates of the reflection point and the signal intensity is a measure for the reflector dimensions. Using this information one can construct an image consisting of individual flat surface fragments.

The method requires special processing of the Rx signals, schematically described in Fig. 16. Pre-processing includes the removal of constant signals (originating from cross-talk between

Tx and Rx antenna at the sensor platform) and distance-dependent amplitude correction of the received signals. After these processing steps a radargram can be drawn for each Rx separately (Fig. 15). Pointwise multiplication of both radargrams increases resolution, because the products of the reflexes occupy a smaller area. All product reflexes have a very similar shape. This allows application of a 2D correlation of the product-radargram with an example pattern, leading to significant improvement of the signal to noise ratio. Experiments have shown that a 2D Gauss-shaped function is a well suited pattern:

$$G(\alpha, r) = \exp\left(-\left(\frac{\alpha - \alpha_0}{\Delta\alpha}\right)^2\right) \cdot \exp\left(-\left(\frac{r - r_0}{\Delta r}\right)^2\right) . \quad (34)$$

α_0 and r_0 are azimuth and radius of the reflex, respectively. For the equipment used in the practical tests (UWB radar 3.5-10.5 GHz, double-ridge horn antenna) the best parameters were $\Delta\alpha = 8.5^\circ$ and $\Delta r = 55$ mm. Afterwards a threshold detector isolates individual reflexes. A table of these reflexes is created. Then 3 parameters are extracted from each reflex : α_0 , r_0 , and the amplitude. Finally the image map is drawn (Fig. 17(c)). The detected reflex centers are marked with small points while the small bars are aligned along the surface orientation. The lengths of the bars are proportional to the signal amplitude. The image generated in this way comes already close to a schematic representation of the object surfaces (Fig. 17(d)).

6. Conclusions

UWB sensor networks can be used for rough imaging of the environment. Measurement results, presented e.g. in Fig. 9 and 17, demonstrate that the shape of simple objects or the structure of a room can be imaged with sufficient quality.

Methods which have been described elsewhere explicitly (e.g.4.3) were mentioned only briefly. New methods (especially chapter 5) were explained in more detail.

The methods presented in this article are especially useful for imaging of interiors. Special applications, e.g. through-wall imaging, have not been mentioned. 3D imaging in a sensor network doesn't seem to be a realistic issue. This would require time-consuming scanning of a 2D surface.

The subject is still under development. Some of the tasks that must be solved by future research are:

- Completely wireless operation of the imaging network must be achieved by introduction of wireless node synchronization.
- The time for data acquisition must be reduced, i.e. methods must be developed that generate an image from a smaller amount of raw data.
- Image artefacts must be reduced, e.g. by improved migration algorithms.

Imaging in UWB sensor networks can become part of surveillance systems with these improvements.

7. References

- Federal Communications Commission, (2002). "Revision of part 15 of the Communication's Rules", *FCC 02-48*, April 2002, pp. 1-174. <http://hraunfoss.fcc.gov>
- Foo, S. & Kashyap, S., "Cross-correlated back projection for UWB radar imaging", *Proceedings of IEEE Antennas and Propagation Society International Symposium*, pp. 1275-1278, ISBN: 0-7803-8302-8, Monterey, CA, USA, September 2004, IEEE Conference Publishing, Piscataway, NJ, USA.
- Gu, K.; Wang, G. & Li, J., (2004). "Migration based SAR imaging for ground penetrating radar systems", *IEE Proceedings Radar Sonar & Navigation*, Vol. 151, No. 5, November 2004, pp. 317-325, ISSN: 1350-2395.
- Hirsch, O.; Janson, M.; Wiesbeck, W. & Thomä, R. S., (2010). "Indirect Localization and Imaging of Objects in an UWB Sensor Network", *IEEE Transactions on Instrumentation and Measurement*, Vol. 59, No. 11, Nov. 2010, pp. 2949-2957, ISSN: 0018-9456.
- Hussain, M. G. M., (1998). "Ultra-wideband impulse radar - an overview of the principles", *IEEE Aerospace and Electronic Systems Magazine*, Vol.13, No.9, September 1998, pp.9-14, ISSN: 0885-8985.
- Luediger, H. & Kallenborn, R., (2009). "Generic UWB Regulation in Europe", *Frequenz, Journal of RF-Engineering and Telecommunications*, Vol.63, No.9-10, Sept./Oct. 2009, pp.172-174, ISSN: 0016-1136.
- Margrave, F. G., (2001). *Numerical Methods of Exploration Seismology with algorithms in MATLAB*, http://www.crewes.org/ResearchLinks/FreeSoftware/EduSoftware/NMES_Margrave.pdf.
- Oliver, C. J., (1989). "Synthetic-aperture radar imaging", *Journal of Physics D: Applied Physics*, Vol.22, No. 7, July 1989, pp. 871-890, doi: 10.1088/0022-3727/22/7/001.
- Patwari, N.; Ash, J.N.; Kyperountas, S.; Hero, A.O., III; Moses, R.L.; Correal, N.S., (2005). "Locating the nodes", *IEEE Signal Processing Magazine*, Vol. 22, No. 4, June 2005, pp. 54-69, ISSN: 1053-5888.
- Rong, P. & Sichiitiu, M. L., (2006). "Angle of Arrival Localization for Wireless Sensor Networks", *Proceedings of SECON 2006*, pp. 374-382, ISBN: 1-4244-0626-9, Reston, VA, USA, September 2006, IEEE Catalog Number: 06EX1523.
- Sachs, J.; Peyerl, P.; Zetik, R. & Crabbe, S., (2003). "M-Sequence Ultra-Wideband-Radar: State of Development and Applications", *Proceedings of Radar 2003*, pp. 224-229, ISBN: 0-7803-7871-7, Adelaide, Australia, September 2003, Causal Productions, Adelaide, Australia.
- Sachs, J. (2004). "M-Sequence Radar", In: *Ground Penetrating Radar*, Daniels, D. J., (Ed.), 2nd ed., pp. 225-236, Inst. of Electrical Engineers, ISBN:0-85296-862-0, Stevenage, U.K. .
- Sayed, A. H.; Tarighat, A.; Khajehnouri, N., (2005). "Network-Based Wireless Location", *IEEE Signal Processing Magazine*, Vol.22, No.4, July 2005, pp.24-40, ISSN: 1053-5888.
- Schwarz, U.; Thiel, F.; Seifert, F.; Stephan, R. & Hein, M. A., (2010). "Ultra-Wideband Antennas for Magnetic Resonance Imaging Navigator Techniques", *IEEE Trans. on Antennas and Propagation*, vol. 58, No. 6, June 2010, pp.2107-2112, ISSN: 0018-926X.
- Serpedin, E. & Chaudhari, Q. M. (2009). *Synchronization in Wireless Sensor Networks: Parameter Estimation, Performance Benchmarks and Protocols*, Cambridge University Press, ISBN: 978-0-521-76442-1, Cambridge, UK.
- Stoica, P. & Li, J., (2006). "Lecture Notes - Source Localization from Range-Difference Measurements", *IEEE Signal Processing Magazine*, Vol.23, No.6, November 2006, pp.63-66, ISSN: 1053-5888.

- Stolt, R. H., (1978). "Migration by Fourier Transform", *Geophysics*, Vol.43, No.1, February 1978, pp.23-48, ISSN: 0016-8033.
- Thomä, R. S.; Hirsch, O.; Sachs, J. & Zetik, R., (2007). "UWB Sensor Networks for Position Location and Imaging of Objects and Environments", *Proceedings of the 2nd European Conference on Antennas and Propagation (EuCAP2007)*, pp. 1-9, ISBN: 978-0-86341-842-6, Edinburgh, U.K., November 2007, IET Conferences, London, U.K.
- Yang, Y. & Yang, K., (2006). "Time Synchronization for Wireless Sensor Networks using the Principle of Radar Systems and UWB Signals", *Proceedings of IEEE International Conference on Information Acquisition 2006*, pp. 160-165, ISBN: 1-4244-0528-9, Weihai, China, August 2006, IEEE Conference Publishing, Piscataway, NJ, USA.
- Zetik, R.; Sachs, J. & Thomä, R., (2005) "Modified Cross-Correlation Back Projection for UWB Imaging: Numerical Examples", *Proceedings of IEEE International Conference on Ultra-Wideband*, pp. 650-654, ISBN: 0-7803-9397-X, Zürich, Switzerland, September 2005, IEEE.
- Zetik, R.; Sachs, J. & Thomä, R., (2005) "Modified Cross-Correlation Back Projection for UWB Imaging: Measurement Examples", *Proceedings of the 6th International Scientific Conference on Digital Signal Processing and Multimedia Communications - DSP-MCOM 2005*, pp. 56-59, ISBN: 80-8073-323-6, Kosice, Slovakia, September 2005, Technicka univerzita Kosice, Kosice, Slovakia.
- Zetik, R.; Sachs, J. & Thomä, R., (2010) "Imaging of distributed objects in UWB sensor networks", In: *Short Pulse Electromagnetics 9*, Sabath, F.; Giri, D. ; Rachidi, F. & Kaelinpp, A. (Ed.), pp. 97-104, Springer-Verlag New York Inc, ISBN: 9780387778440, New York, NY, USA.



Wireless Sensor Networks: Application-Centric Design

Edited by Yen Kheng Tan

ISBN 978-953-307-321-7

Hard cover, 492 pages

Publisher InTech

Published online 14, December, 2010

Published in print edition December, 2010

Over the past decade, there has been a prolific increase in the research, development and commercialisation of Wireless Sensor Networks (WSNs) and their associated technologies. WSNs have found application in a vast range of different domains, scenarios and disciplines. These have included healthcare, defence and security, environmental monitoring and building/structural health monitoring. However, as a result of the broad array of pertinent applications, WSN researchers have also realised the application specificity of the domain; it is incredibly difficult, if not impossible, to find an application-independent solution to most WSN problems. Hence, research into WSNs dictates the adoption of an application-centric design process. This book is not intended to be a comprehensive review of all WSN applications and deployments to date. Instead, it is a collection of state-of-the-art research papers discussing current applications and deployment experiences, but also the communication and data processing technologies that are fundamental in further developing solutions to applications. Whilst a common foundation is retained through all chapters, this book contains a broad array of often differing interpretations, configurations and limitations of WSNs, and this highlights the diversity of this ever-changing research area. The chapters have been categorised into three distinct sections: applications and case studies, communication and networking, and information and data processing. The readership of this book is intended to be postgraduate/postdoctoral researchers and professional engineers, though some of the chapters may be of relevance to interested master's level students.

How to reference

In order to correctly reference this scholarly work, feel free to copy and paste the following:

Ole Hirsch, Rudolf Zetik and Reiner Thomä (2010). Imaging in UWB Sensor Networks, Wireless Sensor Networks: Application-Centric Design, Yen Kheng Tan (Ed.), ISBN: 978-953-307-321-7, InTech, Available from: <http://www.intechopen.com/books/wireless-sensor-networks-application-centric-design/imaging-in-uwbsensor-networks>

INTECH
open science | open minds

InTech Europe

University Campus STeP Ri
Slavka Krautzeka 83/A
51000 Rijeka, Croatia
Phone: +385 (51) 770 447

InTech China

Unit 405, Office Block, Hotel Equatorial Shanghai
No.65, Yan An Road (West), Shanghai, 200040, China
中国上海市延安西路65号上海国际贵都大饭店办公楼405单元
Phone: +86-21-62489820

Fax: +385 (51) 686 166
www.intechopen.com

Fax: +86-21-62489821

© 2010 The Author(s). Licensee IntechOpen. This chapter is distributed under the terms of the [Creative Commons Attribution-NonCommercial-ShareAlike-3.0 License](#), which permits use, distribution and reproduction for non-commercial purposes, provided the original is properly cited and derivative works building on this content are distributed under the same license.